Silver-mean canonical quasicrystalline-generated phononic waveguides

A.K.M. Farhat[1], L. Morini[1] and M. Gei[2]

[1]*School of Engineering, Cardiff University, The Parade, Cardiff CF24 3AA, UK.*
[2]*Department of Engineering and Architecture, University of Trieste, via A. Valerio 6/1, I-34127 Trieste, Italy.*
E-mail: massimiliano.gei@dia.units.it

December 6, 2021

Abstract

We investigate propagation of harmonic axial waves in a class of periodic two-phase phononic rods whose elementary cells are designed adopting the quasicrystalline *silver mean* Fibonacci substitution rule. The stop-/pass-band spectra of this family are studied with the aid of a trace-map formalism which provides a geometrical interpretation of the recursive rule governing traces of the relevant transmission matrices: the traces of two consecutive elementary cells can be represented as a point on a surface defined by an invariant function of the circular frequency, and the recursivity implies the description of an orbit on the surface. We show that, for a sub-class of *silver mean*-generated waveguides, the orbits predicted by the trace map at specific frequencies are periodic. The configurations for which this occurs, called *canonical*, are also associated with periodic stop-/pass-band diagrams along the frequency domain. Several types of periodic orbits exist and each corresponds to a self-similar portion of the dynamic spectra whose scaling law can be studied by linearising the trace map in the neighbourhood of the orbit. The obtained results provide both a new piece of theory to better understand the behaviour of classical two-phase composite periodic waveguides and an important advancement towards design and realisation of phononic quasicrystalline-based metamaterials.

Keywords: Silver-mean Fibonacci sequence, phononic waveguide, quasicrystalline metamaterial, band gap, Kohmoto's invariant.

1 Introduction

In the last twenty years, wave propagation in mechanical metamaterials and their applications in different areas of structural and mechanical engineering have attracted an increasing interest from the scientific community. Many different phononic composites and structures have been designed and tested with the aim of achieving and controlling several innovative dynamical phenomena, such as frequency filtering [1, 2, 3], wave focussing [4, 5], cloaking [6, 7], negative refraction [8, 9, 10] and non-reciprocal propagation [11, 12].

Recently, elastodynamics of composite beams following a quasiperiodic pattern has gained considerably attention (see e.g. [13, 14, 15, 16]). In particular, the non-standard dispersive properties of a class of two-phase periodic structured rods whose unit cells are generated according to the Fibonacci substitution rule have been presented [13, 17, 18]. This class belongs to the subset of *quasicrystalline* media [19, 20] and portions of Floquet-Bloch frequency spectra of its members display a self-similar pattern which scales according to factors linked to an invariant function, the so-called Kohmoto's invariant [21].

In this paper, we generalise these concepts to study the dynamical properties of another type of periodic quasicrystalline-generated waveguide, namely, that composed of elementary cells conceived by adopting a generalised Fibonacci substitution rule based on the binary sequence, commonly known as *silver mean* [21, 22]. By considering harmonic axial wave propagation, we show that the corresponding Floquet-Bloch dynamic spectra can be fully determined by studying the behaviour of the traces of the transmission matrices of three 'adjacent' elementary cells, which are related through recursive relationships. These connections allow us to apply the trace-map formalism [23], which provides the geometrical representation of the traces as coordinates of points which describe orbits on a surface defined by the Kohmoto's invariant. Those orbits are studied in detail, to find that, for a sub-class of silver-mean waveguides, they are periodic at specific frequencies, called *canonical* frequencies, in analogy to those determined for the standard Fibonacci sequence by Gei et al. [24]. In particular, there exist three types of canonical frequencies and each of them can be associated with a well-defined configuration of the elementary cell called, likewise, *canonical configuration*.

Each of the three families of canonical configurations is characterised by self-similar properties of the layouts of stop and pass bands, a feature that can be linked to the periodic orbits on the invariant surface. By means of a linearisation procedure of the trace map, we obtain analytical scaling factors governing the different self-similar ranges of the spectra for all three families of canonical rods. The scaling factors could be used to predict, design and optimise the unique filtering properties of a two-phase silver-mean

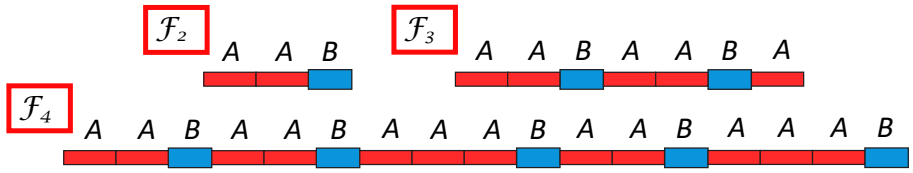

Figure 1: Representative elementary cells for periodic silver-mean phononic rods: $\mathcal{F}_2 = (AAB)$, $\mathcal{F}_3 = (AABAABA)$ and $\mathcal{F}_4 = (AABAABAAABAABAAAB)$.

generated structured rods.

2 Analysis of wave propagation

We introduce a particular class of infinite, one-dimensional, two-component quasiperiodic phononic rods consisting of a repeated elementary cell where two distinct phases, say A and B, are arranged in series according to the so-called *Silver Mean* (SM) sequence. The repetition of the fundamental cell implies global periodicity along the axis and then the possibility of applying Floquet-Bloch technique to investigate propagation of harmonic elastic waves in these systems. The two-component SM sequence belongs to the family of patterns commonly known as one-dimensional *generalised Fibonacci* tilings [23] and is based on the following substitution rule:

$$A \to AAB, \quad B \to A. \tag{1}$$

Expression (1) implies that element of $i-$th order of the sequence ($i = 0, 1, 2, \dots$), here denoted by $\mathcal{F}_i$, obeys the recursive rule

$$\mathcal{F}_i = \mathcal{F}_{i-1}^2 \mathcal{F}_{i-2}, \tag{2}$$

where the initial condition is $\mathcal{F}_0 = B$ and $\mathcal{F}_1 = A$ (in Fig. 1, elementary cells representing $\mathcal{F}_2$, $\mathcal{F}_3$ and $\mathcal{F}_4$ are sketched, where the notation $\mathcal{F}_i$ will also indicate the i-th elementary cell of the structured rod). The total number of elements of $\mathcal{F}_i$ corresponds to the generalised Fibonacci number $\tilde{n}_i$, given by the recursive relation $\tilde{n}_i = 2\tilde{n}_{i-1} + \tilde{n}_{i-2}$, with $i \geq 2$ and $\tilde{n}_0 = \tilde{n}_1 = 1$. The limit $\tilde{n}_{i+1}/\tilde{n}_i$ for $i \to \infty$ corresponds to the *silver mean ratio* $\sigma_s = (1 + \sqrt{2}) \cong 2.414$.

Further in the text, we will refer to those structured elements as SM rods. According to the general criterion for the classification of the one-dimensional quasiperiodic patterns proposed in [25], the SM arrangement is *quasicrystalline*. Quasicrystalline media possess specific properties that make them an intermediate class between periodic crystals and random amorphous solids [26, 27]. An example of these interesting and intriguing features is the self-similarity of the distribution of stop and pass bands detected for phononic

waveguides arranged according to several generalised Fibonacci sequences [17, 24]. *The focus of the paper is on the analysis of harmonic axial wave propagation in SM rods.* We will show that the spectrum of this class of structures is characterised by specific self-similar properties, different from those pertaining to other quasicrystalline-generated waveguides. In particular, we will illustrate how these unique features are closely related to the properties of the Floquet-Bloch dispersion relationship, reported in this Section.

Let us introduce the geometrical and physical properties of phases A and B. The lengths of the two elements are indicated respectively with l_A and l_B, while S_X, E_X, and ϱ_X ($X \in \{A, B\}$) denote cross-section area, Young's modulus and mass density per unit of volume of each element, respectively. For both segments, we define the displacement function along the rod $u(z)$ and the axial force $N(z) = ESu'(z)$, where z is the longitudinal axis. The governing equation of harmonic axial waves in each phase is

$$u''_X(z) + Q_X\,\omega^2 u_X(z) = 0, \tag{3}$$

where ω is the circular frequency (simply the 'frequency' in the following) and $Q_X = \varrho_X/E_X$ corresponds to the reciprocal of the square of the speed of propagation of longitudinal waves in material X. The general solution for eq. (3) assumes the form

$$u_X(z) = C_X \sin(\sqrt{Q_X}\,\omega z) + D_X \cos(\sqrt{Q_X}\,\omega z), \tag{4}$$

where C_X and D_X are integration constants, to be determined by the boundary conditions.

To obtain the dispersion diagram of the periodic rod, displacement and axial force at the right-hand boundary of the elementary cell, respectively u_r and N_r, have to be identified in terms of those at the left-hand boundary, respectively u_l and N_l, as

$$\mathbf{U}_r = \mathbf{T}_i \mathbf{U}_l, \tag{5}$$

where $\mathbf{U}_j = [u_j \;\; N_j]^T$ ($j = r, l$) and $\mathbf{T}_i$ is the transmission matrix [28] of the cell $\mathcal{F}_i$. The latter is the result of the product $\mathbf{T}_i = \prod_{p=1}^{\tilde{n}_i} \mathbf{T}^X$, where $\mathbf{T}^X$ ($X \in \{A, B\}$) is the transmission matrix relating quantities across a single element, given by

$$\mathbf{T}^X = \begin{bmatrix} \cos(l_X\sqrt{Q_X}\,\omega) & \dfrac{\sin(l_X\sqrt{Q_X}\,\omega)}{E_X S_X \sqrt{Q_X}\,\omega} \\ -E_X S_X \sqrt{Q_X}\,\omega \sin(l_X\sqrt{Q_X}\,\omega) & \cos(l_X\sqrt{Q_X}\,\omega) \end{bmatrix}. \tag{6}$$

Transmission matrices $\mathbf{T}_i$ are unimodular, i.e. $\det \mathbf{T}_i = 1$, and follow the recursion rule

$$\mathbf{T}_{i+1} = \mathbf{T}_{i-1}\mathbf{T}_i^2, \tag{7}$$

with $\mathbf{T}_0 = \mathbf{T}^B$ and $\mathbf{T}_1 = \mathbf{T}^A$.

The Floquet-Bloch condition requires that $\mathbf{U}_r = \exp(\mathrm{i}K)\mathbf{U}_l$, so that, by combining this with eq. (5), the dispersion equation takes the form $\det[\mathbf{T}_i - \exp(\mathrm{i}K)\mathbf{I}] = 0$, or, in explicit terms[1],

$$K = \arccos\left(\frac{\mathsf{tr}\mathbf{T}_i}{2}\right). \tag{8}$$

The solution to eq. (8) provides the complete Floquet-Bloch spectrum and allows to obtain the mentioned stop-/pass-band pattern of the waveguides at varying index i. In particular, waves propagate when $|\mathsf{tr}\mathbf{T}_i| < 2$, stop bands correspond to $|\mathsf{tr}\mathbf{T}_i| > 2$, whereas $|\mathsf{tr}\mathbf{T}_i| = 2$ is the condition for standing waves. In finite-size waveguides composed of a finite number of elementary cells, stop bands (resp. pass bands) are the range of frequencies when the reflection (resp. transmission) coefficient approaches one [28], a property that will be verified later in the text with a couple of *ad hoc* examples.

3 Trace map and Kohmoto's invariant

This Section is devoted to the study of the properties of trace $\mathsf{tr}\mathbf{T}_i$ and how these features affect the frequency spectrum of SM rods. A nonlinear recursive relationship connecting traces for consecutive fundamental cells $\mathcal{F}_i$ is introduced. An invariant function defining a three-dimensional surface, the so-called Kohmoto's surface, is found for this map. At any frequency, the evolution of the traces corresponds to an orbit on this surface. By means of this analysis, we introduce a special sub-class of structures, characterized by –closed– periodic orbits on the Kohmoto's surface associated with particular values of the frequency.

3.1 Nonlinear map and Kohmoto's invariant

General recursive relations for the traces of unimodular 2×2 transmission matrices of generalised Fibonacci chains have been derived in [23] in terms of Chebyshev polynomials of first and second kind. Specialising these expressions to the case SM, we derive the pair of equations

$$\begin{cases} x_i = x_{i-1}t_i - x_{i-2}, \\ t_{i+1} = x_i x_{i-1} - t_i, \end{cases} \quad \text{with} \quad i \geq 2, \tag{9}$$

where $x_i = \mathsf{tr}\mathbf{T}_i$ and $t_i = \mathsf{tr}(\mathbf{T}_{i-2}\mathbf{T}_{i-1})$. Through the new set of variables

$$\tilde{x}_i = t_{i+2},\ \tilde{y}_i = x_{i+1},\ \tilde{z}_i = x_i \tag{10}$$

[1]The reader is referred to [29, 30] for a generalisation of the dispersion equation to the case of bi-coupled systems in which the square transmission matrix is of order 4.

and its substitution into expression (9), the following nonlinear map determining the evolution of x_i and t_i is obtained

$$\mathcal{T}:\mathbb{R}^3\to\mathbb{R}^3,\ \mathcal{T}(\tilde{x}_i,\tilde{y}_i,\tilde{z}_i)=(\tilde{x}_{i+1},\tilde{y}_{i+1},\tilde{z}_{i+1})=\left(\tilde{x}_i\tilde{y}_i^2-\tilde{y}_i\tilde{z}_i-\tilde{x}_i,\ \tilde{x}_i\tilde{y}_i-\tilde{z}_i,\ \tilde{y}_i\right), \quad (11)$$

where the initial conditions are given by

$$\begin{aligned}\tilde{z}_0=x_0&=2\cos\left(l_B\sqrt{Q_B}\omega\right),\qquad \tilde{y}_0=x_1=2\cos\left(l_A\sqrt{Q_A}\omega\right),\\ \tilde{x}_0=t_2&=2\cos\left(l_A\sqrt{Q_A}\omega\right)\cos\left(l_B\sqrt{Q_B}\omega\right)-\beta\sin\left(l_A\sqrt{Q_A}\omega\right)\sin\left(l_B\sqrt{Q_B}\omega\right),\end{aligned} \quad (12)$$

where the impedance mismatch β takes the form

$$\beta=\frac{S_A^2E_A^2Q_A+S_B^2E_B^2Q_B}{S_AE_AS_BE_B\sqrt{Q_AQ_B}}. \quad (13)$$

Since (11) is a differentiable map, its jacobian, namely

$$\mathbf{J}=\frac{\partial(\tilde{x}_{i+1},\tilde{y}_{i+1},\tilde{z}_{i+1})}{\partial(\tilde{x}_i,\tilde{y}_i,\tilde{z}_i)}=\begin{bmatrix}\tilde{y}_i^2-1 & 2\tilde{x}_i\tilde{y}_i-\tilde{z}_i & -\tilde{y}_i\\ \tilde{y}_i & \tilde{x}_i & -1\\ 0 & 1 & 0\end{bmatrix}, \quad (14)$$

can be evaluated, showing that $\det\mathbf{J}=-1$. Through a little algebra we can also demonstrate that, similarly to all precious-mean sequences [17], the quantity

$$I(\omega)=\tilde{x}_i^2+\tilde{y}_i^2+\tilde{z}_i^2-\tilde{x}_i\tilde{y}_i\tilde{z}_i-4=(\beta^2-4)\sin^2\left(l_A\sqrt{Q_A}\omega\right)\sin^2\left(l_B\sqrt{Q_B}\omega\right) \quad (15)$$

is an invariant of the map. This means that at a given frequency ω, the value $I(\omega)$ is independent of the order i of the sequence $\mathcal{F}_i$. In the three-dimensional space spanned by the cartesian coordinate system $O\tilde{x}\tilde{y}\tilde{z}$, the cubic

$$\tilde{x}^2+\tilde{y}^2+\tilde{z}^2-\tilde{x}\tilde{y}\tilde{z}-4=I(\omega) \quad (16)$$

is the equation of a two-dimensional manifold that was named by the authors *Kohmoto's surface*. For a given frequency ω, all points detected by the triad $R_i=(\tilde{x}_i,\tilde{y}_i,\tilde{z}_i)$ and generated through (11) can be mapped onto the surface defined by eq. (16). By taking into account that $\tilde{y}_i$, $\tilde{z}_i$ correspond to real traces (see eq. (10)), the position of point R_i may reveal if, at a given ω, structures $\mathcal{F}_i$ and $\mathcal{F}_{i+i}$ are/are not in a pass band; in particular, i) both $\mathcal{F}_i$ and $\mathcal{F}_{i+i}$ are in a pass band if $\{|x_i|,|x_{i+1}|\}<2$; ii) both are in a stop band if $\{|x_i|,|x_{i+1}|\}>2$.

The four plots in Fig. 2 refer to a prototype SM rod whose parameters[2] will be further described in the next section, at a dimensionless frequency $l_A\sqrt{Q_A}\omega=1.548$.

[2] $Q_B/Q_A=1$, $E_B/E_A=1$, $S_B/S_A=1/2$, $l_B/l_A=5$.

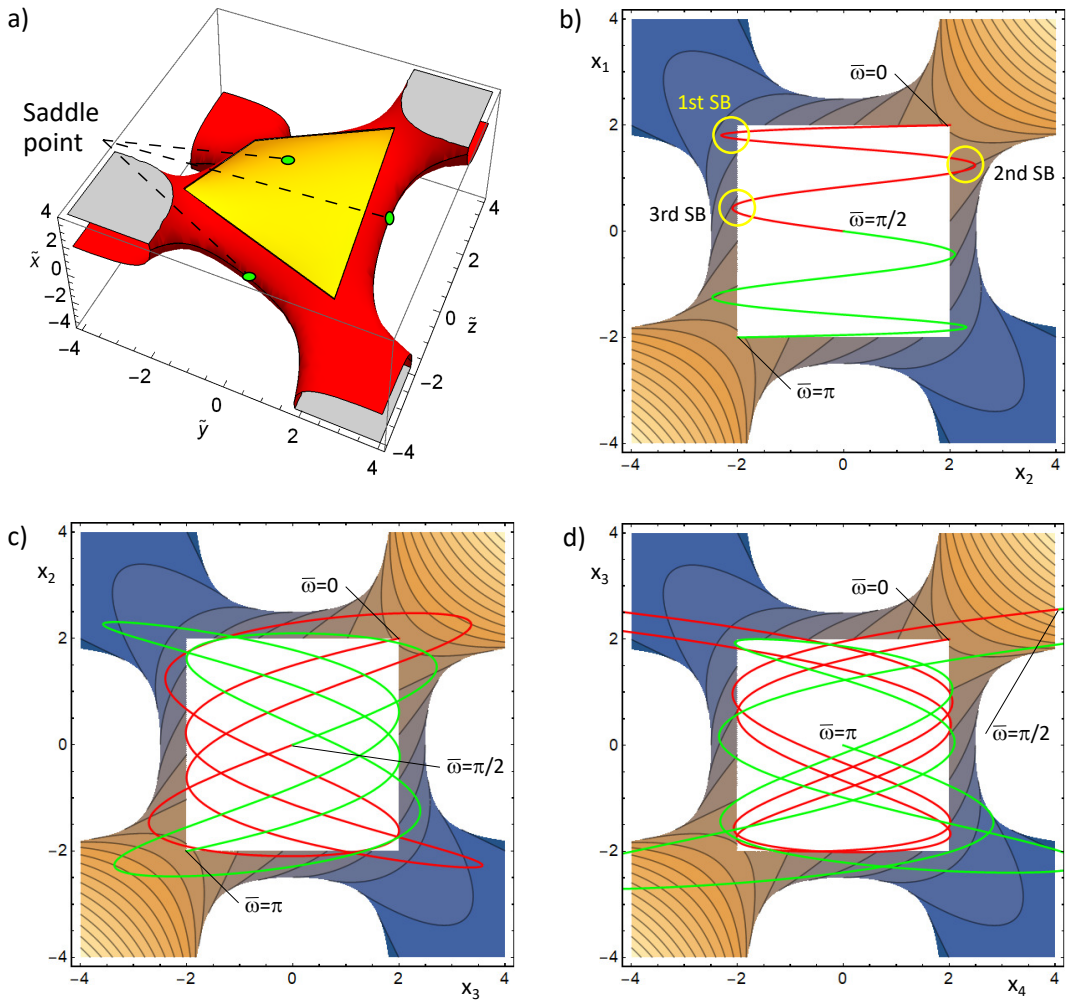

Figure 2: Kohmoto's surface for a SM rod whose parameters are $Q_B/Q_A = 1$, $E_B/E_A = 1$, $S_B/S_A = 1/2$, $l_B/l_A = 5$. a) 3-dimensional representation where three out of six saddle points are indicated. b), c), d) sketches in the plane $(\tilde{y}, \tilde{z})$, where the reported trajectories have parametric equations: b) $(x_2(\omega), x_1(\omega))$; c) $(x_3(\omega), x_2(\omega))$; d) $(x_4(\omega), x_3(\omega))$. In all plots of b), c), d) the red line is for $\bar{\omega} = l_A\sqrt{Q_A}\omega \in [0, \pi/2]$, the green one is for $\bar{\omega} \in [\pi/2, \pi]$. SB stands for 'stop band'.

In Fig. 2a), the Kohmoto's surface in the 3-dimensional space $O\tilde{x}\tilde{y}\tilde{z}$ is represented; the yellow domain corresponds to $\{|x_i|, |x_{i+1}|\} < 2$ and three out of the six saddle points possessed by the surface are indicated with a green dot. In Figs. 2b) c) d), the same surface is sketched in the subspace $O\tilde{y}\tilde{z}$, where the white squares in the centre of the three panels match, in projection, the yellow sub-surface in part a). Therefore, a point $\hat{R}_i(\omega) = (\tilde{y}_i, \tilde{z}_i) = (x_{i+1}(\omega), x_i(\omega))$ belonging to these squares indicates that the circular frequency ω for both $\mathcal{F}_i$ and $\mathcal{F}_{i+i}$ lies in a pass band.

The trajectories sketched in the three plots of the same figure have parametric equations $(x_2(\omega), x_1(\omega))$ (b), $(x_3(\omega), x_2(\omega))$ (c) and $(x_4(\omega), x_3(\omega))$ (d). All trajectories start

at the corner of coordinates $(2, 2)$ that corresponds to $\omega = 0$, then the red line covers the range $\bar{\omega} = l_A\sqrt{Q_A}\omega \in [0, \pi/2]$ after which the green line follows, reaching $\bar{\omega} = \pi$. The trajectory then continues with a pattern that the reader can easily envisage. In b) the represented trajectory describes all frequencies $\bar{\omega} \in [0, +\infty[$ as the continuation for $\bar{\omega} \in [\pi, 2\pi]$ corresponds to the same path, but travelling in the opposite direction, and so on. Moreover, as expected, $|x_1| \leq 2$, $\forall\omega$, as $\mathcal{F}_1$ is a homogeneous waveguide with any stop band in its spectrum. In the same part b), the first three low-frequency stop bands (SB) for $\mathcal{F}_2$ are indicated. Parts c) and d) can be similarly interpreted, in particular the location of stop bands can be spotted following the curved lines, however the complexity increases at increasing index i of the sequence. Note, for instance, where is the point of transition between red and green lines (i.e. $\bar{\omega} = \pi/2$) in Fig. 2d).

3.2 Periodic orbits on Kohmoto's surface and canonical configurations

By recalling the analyses performed by Morini and Gei [17] and Gei et al. [24], there are essentially three kinds of orbits which can be followed by points R_i as a consequence of the iteration map (11): (*i*) periodic orbits, (*ii*) non-periodic bounded orbits and (*iii*) escaping orbits. At any frequency ω, corresponding to a determinate Kohmoto's surface (16), the type of orbit is uniquely determined by the initial point $R_0 = (\tilde{x}_0, \tilde{y}_0, \tilde{z}_0)$ whose coordinates are given by expressions (12).

We focus now our attention on periodic orbits and in particular to the investigation of specific configurations for SM periodic rods. Guided by the previous work on standard, *golden mean* (GM) rods, we indicate with P_j $(j = 1, \ldots, 6)$ the six saddle points of the manifold (16) whose coordinates are $P_{1,4} = (0, 0, \pm\alpha_1)$, $P_{3,6} = (0, \mp\alpha_2, 0)$, $P_{2,5} = (\pm\alpha_3, 0, 0)$, where the top sign is associated with the lowest index and α_k $(k = 1, 2, 3)$ depend on the specific case. As anticipated, in Fig. 2a) three out of six saddle points are sketched. We then wonder if any periodic orbit joining those points might exist. The answer can be found by imposing, at some frequencies,

$$\tilde{y}_0 = \tilde{z}_0 = 0, \tag{17}$$

or

$$\tilde{x}_0 = \tilde{z}_0 = 0, \quad \text{or} \quad \tilde{x}_0 = \tilde{y}_0 = 0. \tag{18}$$

The requirements (17) and (18) can be fulfilled only for particular classes of layouts, namely the *canonical* (SM) layouts, in analogy to the definition proposed by Gei et al. [24] for GM sequences. By substituting expressions (12) into condition (17), the following relationship between physical and geometrical properties of phases A and B are derived,

i.e. ($\mathcal{C} = l_B/l_A\sqrt{Q_B/Q_A}$)

$$\mathcal{C}_1 = \frac{1+2j}{1+2k}, \quad \text{with } j,k \in \mathbb{N}. \tag{19}$$

Similarly, by using (12) into eqs. (18), we obtain

$$\mathcal{C}_2 = \frac{1+2j}{2q}, \quad \mathcal{C}_3 = \frac{2q}{1+2k}, \quad \text{with } j,k,q \in \mathbb{N}, \tag{20}$$

respectively. $\mathcal{C}_1$, $\mathcal{C}_2$ and $\mathcal{C}_3$ are the *canonical ratios*. Each of them identifies a family of canonical SM rods (no. 1, no. 2 and no. 3, respectively). In turn, the *canonical frequencies* are given by

$$\omega_{\mathcal{C}_{rn}} = \omega_{\mathcal{C}_r}(1+2n), \qquad \text{with } n \in \mathbb{N},\ r = 1,2,3, \tag{21}$$

where

$$\omega_{\mathcal{C}_1} = \omega_{\mathcal{C}_3} = \frac{\pi}{2l_A\sqrt{Q_A}}(1+2k), \qquad \text{with } k \in \mathbb{N}, \tag{22}$$

$$\omega_{\mathcal{C}_2} = \frac{\pi}{l_A\sqrt{Q_A}}q, \quad \text{with } q \in \mathbb{N}. \tag{23}$$

Eq. (21), with eqs. (22) and (23), identifies the values of the circular frequencies satisfying conditions (17) and (18).

Any arbitrary canonical SM waveguide $\mathcal{F}_i$ displays a *periodic* stop-/pass-band layout whose period depends only on the value of the canonical frequency. In particular, periodicity is enforced by requirements (17) and (18). The least frequency interval where all traces are periodic is $[0, 4\,\omega_{\mathcal{C}_r}]\,(r = 1,2,3)$, as an inspection of the first two equalities in (12) may reveal.

Elements of *Family no. 1* possess features that differ from those characterising the other two families that can be studied together.

Due to rule $(9)_1$ and eq. (17), it turns out that, for Family no. 1, $x_2 = x_1 t_2 - x_0$, an expression which leads to $x_2 = 0$ at the canonical frequencies. Therefore, $x_i(\omega_{\mathcal{C}_{1n}}) = 0, \forall i$, implying that at these frequencies a *waveguide belonging to Family no. 1 always displays a pass band*. Moreover, a two-point periodic orbit is achieved at $\omega_{\mathcal{C}_{1n}}$, namely

$$P_2 = (\beta, 0, 0) \ \xrightarrow{\mathcal{T}}\ P_5 = (-\beta, 0, 0) \ \xrightarrow{\mathcal{T}}\ P_2, \tag{24}$$

or, equivalently, $\mathcal{T}^2(P_{2,5}) = P_{2,5}$. The orbit (24) will be denoted henceforth as $\bar{\mathcal{T}}^2$. Note that $I(\omega_{\mathcal{C}_1}) = I(\omega_{\mathcal{C}_{1n}}) = \beta^2 - 4 > 0$.

For *Families no. 2* and *3*, the invariant evaluated at a canonical frequency always vanishes, i.e. $I(\omega_{\mathcal{C}_{rn}}) = 0$ $(r = 2,3)$. The recursive rule (9) provides a four-point periodic orbit encompassing the four saddle points not involved in $\bar{\mathcal{T}}^2$, namely

$$P_1 = (0,0,2) \ \xrightarrow{\mathcal{T}}\ P_3 = (0,-2,0) \ \xrightarrow{\mathcal{T}}\ P_4 = (0,0,-2) \ \xrightarrow{\mathcal{T}}\ P_6 = (0,2,0) \ \xrightarrow{\mathcal{T}}\ P_1. \tag{25}$$

This orbit will be referred from now on as $\bar{\mathcal{T}}^4$.

Additional periodic orbits can be found at non-canonical frequencies $\hat{\omega}$ such that $I(\hat{\omega}) = 0$. This may occur in a large variety of cases depending on the value of $\mathcal{C}$ that are however not classified here. Nevertheless, the following cases are universal (i.e., valid for all three Families of canonical rods):

(i) the pair $x_0 = x_1 = 2$ can be found at the endpoints of the interval where traces are periodic, namely at $\omega = 0, 4\,\omega_{\mathcal{C}_r}$; therefore, $R_i = (2, 2, 2)$, $\forall i$, corresponding to a *fixed-point* orbit, i.e. $\mathcal{T}(R_i) = R_i$;

(ii) for $\omega = 2\,\omega_{\mathcal{C}_r}$, $x_0 = -x_1 = -2$, then $R_0 = (-2, 2, -2) = R_2 = R_k$, with k even, whereas $R_1 = (-2, -2, 2) = R_3 = R_m$, with m odd; the general rule for this frequency is that the orbit is two-point periodic, i.e. $\mathcal{T}^2(R_{k,m}) = R_{k,m}$.

To illustrate the features of the dispersion diagram for canonical SM rods, the stop-/pass-band layouts are displayed in Figs. 3 and 4 for two prototype examples belonging to Family no. 1 ($\mathcal{C}_1 = 5$) and Family no. 3 ($\mathcal{C}_3 = 2/3$), respectively. In all cases displayed in the paper, $Q_B/Q_A = 1$, $E_B/E_A = 1$, $S_B/S_A = 1/2$, so that $\beta = 2.5$. Therefore, the chosen length ratio l_B/l_A corresponds to $\mathcal{C}$.

In the top part of Fig. 3, the invariant $I(\omega)$ is sketched in the interval in which the function itself – but not the traces (!), see above – is periodic, namely $[0, 2\,l_A\sqrt{Q_A}\,\omega_{\mathcal{C}_1}]$. While, on the one hand, it is confirmed that, as predicted, $I(\omega_{\mathcal{C}_1}) > 0$ (its value is 2.25), on the other hand, in addition to cases classified as (i) and (ii) just above, at $\hat{\bar{\omega}} = l_A\sqrt{Q_A}\hat{\omega} = p\,\pi/5$ ($p = 1, \ldots, 4$) the function vanishes. There, periodic orbits may be found which are all 6-point periodic. However, the initial point R_0 of each orbit depends on p: for instance, for $\hat{\bar{\omega}} = \pi/5$, $R_0 = (-\phi, \phi, -2)$, where ϕ is the golden ratio ($\phi = (\sqrt{5} + 1)/2$), whereas for $\hat{\bar{\omega}} = 2\pi/5$, $R_0 = (1/\phi, 1/\phi, 2)$.

In the bottom part of the figure, the layout of stop/pass bands is sketched for sequences $\mathcal{F}_2$ to $\mathcal{F}_4$. A higher index i could have been studied for the whole interval, but the increasing smallness of the widths of the bands in certain frequency ranges would have made the diagram illegible. However, a close-up view of the layout for $\mathcal{F}_4$ to $\mathcal{F}_6$ in the neighbourhood of the canonical frequency is included to highlight the local self-similar pattern of the spectra. It is evident that in the scaled domain, $\mathcal{F}_4$–$\mathcal{F}_5$–$\mathcal{F}_6$ show a sequence of pass bands very similar to that pertaining to $\mathcal{F}_2$–$\mathcal{F}_3$–$\mathcal{F}_4$ (sketched in red) in the whole domain. The 'match' between patterns improves at increasing index i; the value of the scaling factor will be determined with the method developed in Sect. 4.

In Fig. 4, the function $I(\omega)$ in the same interval (i.e. $[0, 2\,l_A\sqrt{Q_A}\omega_{\mathcal{C}_3}]$) is reported. Differently than Fig. 3, at the canonical frequency the invariant vanishes, namely $I(\omega_{\mathcal{C}_3}) = 0$, and this also occurs for $\hat{\bar{\omega}} = \pi, 2\pi$. All the three frequencies are loci where 4-point periodic orbits are present with initial point being equal to $R_0 = (1, -2, -1)$ for $\hat{\bar{\omega}} = \pi$ and $R_0 = (-1, 2, -1)$ for $\hat{\bar{\omega}} = 2\pi$.

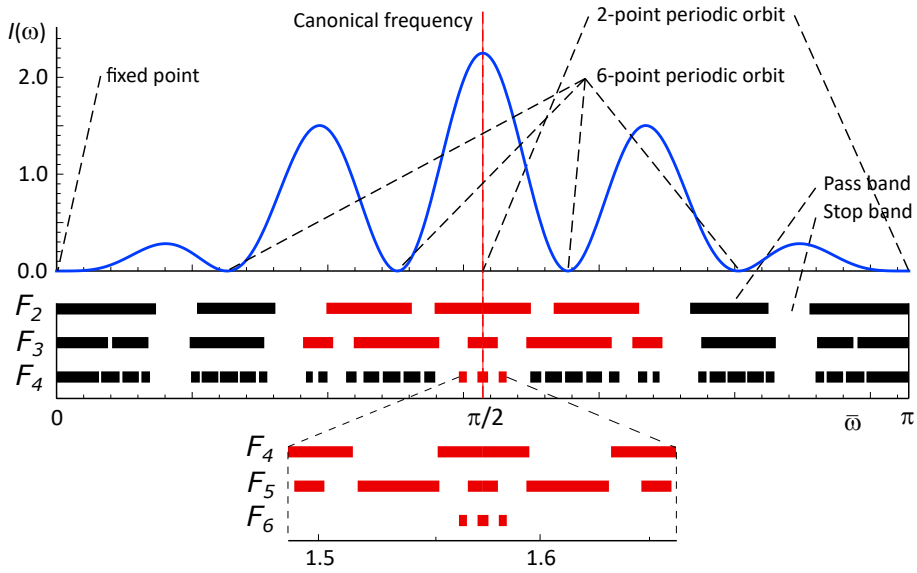

Figure 3: Canonical SM rod with $\mathcal{C}_1 = 5$ (Family no. 1). Top: sketch of the invariant $I(\omega)$ in the domain $[0, 2\,l_A\sqrt{Q_A}\omega_{\mathcal{C}_1}]$, the frequencies at which periodic orbits occur are indicated; bottom: stop-/pass-band layout in the same interval for sequences $\mathcal{F}_2$ to $\mathcal{F}_4$ and close-up view of the layout for $\mathcal{F}_4$ to $\mathcal{F}_6$ in the neighbourhood of the canonical frequency. The dimensionless canonical frequency is $\pi/2$.

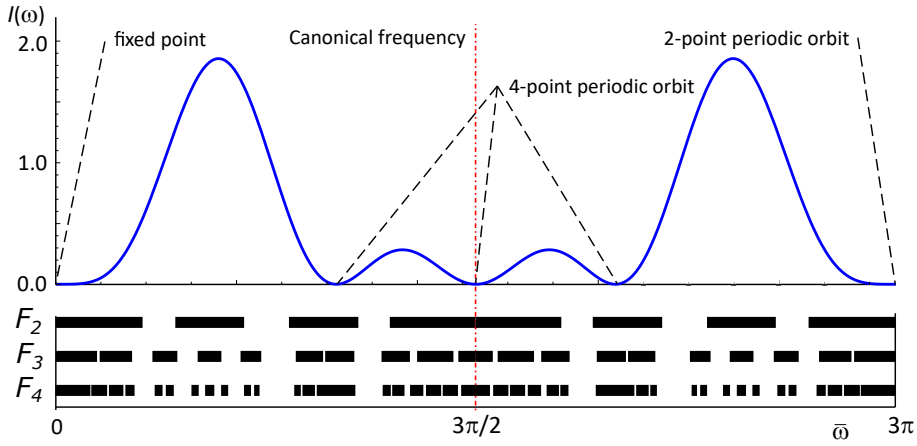

Figure 4: Canonical SM rod with $\mathcal{C}_3 = 2/3$ (Family no. 3). Top: sketch of the invariant $I(\omega)$ in the domainl $[0, 2\,l_A\sqrt{Q_A}\omega_{\mathcal{C}_3}]$ where the frequencies at which periodic orbits occur are indicated; bottom: stop-/pass-band layout in the same interval for sequences $\mathcal{F}_2$ to $\mathcal{F}_4$. The dimensionless canonical frequency is $3\pi/2$.

In order to give the reader an insight into the diagrams illustrated in Figs. 3 and 4, we consider two finite waveguides composed of six elementary cells $\mathcal{F}_2$ and $\mathcal{F}_4$, respectively, belonging to Family no. 1. They join two semi-infinite, identical outer media whose elastic properties match those of phase A (Fig. 5a)). We expect the system to be able to transmit (resp. reflect) a signal whose frequency belongs to a pass band (resp. stop

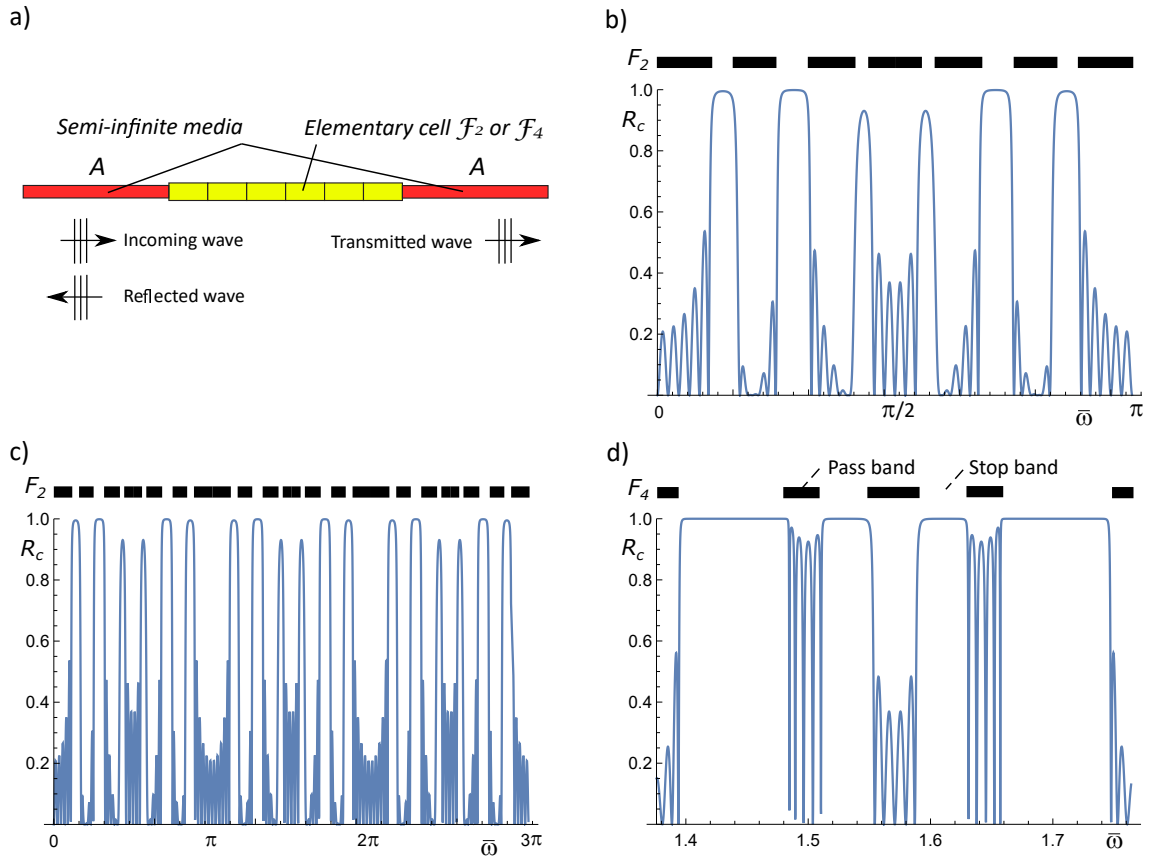

Figure 5: Canonical SM rod with $\mathcal{C}_1 = 5$ (Family no. 1). a) Schematic of the finite-size waveguide; b) plot of the reflection coefficient R_c for elementary cell $\mathcal{F}_2$ for a dimensionless frequency in the interval $[0, 2\,l_A\sqrt{Q_A}\omega_{\mathcal{C}_1}]$; c) same as in b), but in the domain $[0, 6\,l_A\sqrt{Q_A}\omega_{\mathcal{C}_1}]$; d) plot of the reflection coefficient R_c for elementary cell $\mathcal{F}_4$ in the domain $[1.376, 1.764]$.

band). To this end, transmission coefficient T_c and reflection coefficient $R_c = 1 - T_c$ can be calculated following the method presented in [28]. The reflection coefficients for the two problems at hand are displayed in Fig. 5. For $\mathcal{F}_2$, the whole domain $[0, 2\,l_A\sqrt{Q_A}\,\omega_{\mathcal{C}_1}]$ represented in Fig. 3 is analysed in Fig. 5b), whereas for the elementary cell $\mathcal{F}_4$, the range $l_A\sqrt{Q_A}\,\omega \in [1.376, 1.764]$ is analysed in Fig. 5d). In both diagrams, it is evident that R_c approaches 1 in the stop bands, thus confirming that the model of infinite, periodic waveguide provides an excellent estimation of the range of frequencies at which waves cannot propagate. For cell $\mathcal{F}_2$, the reflection coefficient for a domain three times wider than that in Fig. 5b) is reported in Fig. 5c) to show the periodicity of the response of the finite-size device, confirming once again the prediction of the theory of canonical phononic waveguides.

4 Scaling and self-similarity of the frequency spectra of canonical SM rods

In this Section, analytical scaling factors which govern the self-similar pattern of stop- and pass-band layouts of canonical SM rods are obtained through the linearisation of the map (11) about the relevant periodic orbits, i.e. (24) and (25).

4.1 Linearisation of the trace map about saddle points

Following the approach presented in [17] and [24], we can study non-periodic bounded orbits on the Kohmoto's surface as linear perturbations of the periodic orbits defined in the previous Section.

Consider a saddle point $P_{\bar{j}}$ as a point of a $p-$periodic orbit. Let us assume, for a 'small' $\delta\omega$, that $\bar{R}_i = R_i(\omega + \delta\omega)$, where $R_i(\omega) = P_{\bar{j}}$. Then, $\bar{R}_i$ is in the neighbourhood of $P_{\bar{j}}$ and the modulus of the vector $\delta\mathbf{r}_i(\delta\omega) = \bar{R}_i - P_{\bar{j}}$ is small with respect to the value of the non-vanishing coordinate of $P_{\bar{j}}$. On the one hand, by applying p times the transformation $\mathcal{T}$, the exact position of $\bar{R}_{i+p} = \mathcal{T}^p(\bar{R}_i)$ can be established. On the other, due to the smallness of $|\delta\mathbf{r}_i|$, a linearisation of the nonlinear map can be performed such that the position of point $\bar{R}_{i+p}$ can be approximated by $P_{\bar{j}} + \delta\hat{\mathbf{r}}_{i+p}$, where

$$\delta\hat{\mathbf{r}}_{i+p} = \bar{\mathbf{A}}_p \delta\mathbf{r}_i. \tag{26}$$

The operator $\bar{\mathbf{A}}_p$ depends on the orbit and examples in this paper include

$$\bar{\mathbf{A}}_2 = \mathbf{J}(P_5)\mathbf{J}(P_2)$$

for $\bar{\mathcal{T}}^2$ [cf. (24)] and

$$\bar{\mathbf{A}}_4 = \mathbf{J}(P_6)\mathbf{J}(P_4)\mathbf{J}(P_3)\mathbf{J}(P_1)$$

for $\bar{\mathcal{T}}^4$ [cf. (25)], where $\mathbf{J}(P_j)$ is the jacobian matrix (14) evaluated at the saddle point P_j [3].

To proceed further, let us focus on the spectral representations of $\bar{\mathbf{A}}_2$ and $\bar{\mathbf{A}}_4$ that are matrices whose determinants are both unitary. They both share an eigenvalue equal to one that is associated with a unit eigenvector, say $\mathbf{g}^\star$. The remaining two eigenvalues are

$$\kappa_2^{\pm} = -\frac{1}{2}\left[2 + \beta^2 \pm \beta\sqrt{4+\beta^2}\right], \qquad \kappa_4^{\pm} = (2\sqrt{2} \pm 3)^2, \tag{27}$$

respectively, and note that $\kappa_p^+ = 1/\kappa_p^-$ $(p = 2, 4)$ and $\kappa_4^+ = \sigma_s^4$. We indicate the unit eigenvector related to κ_p^+ (resp. κ_p^-) as $\mathbf{g}^+$ (resp. $\mathbf{g}^-$). κ_p^+ is usually much larger than

[3] In the just mentioned examples, $\bar{\mathbf{A}}_2$ and $\bar{\mathbf{A}}_4$ have those expressions if $P_{\bar{j}} = P_2$ and $P_{\bar{j}} = P_1$, respectively.

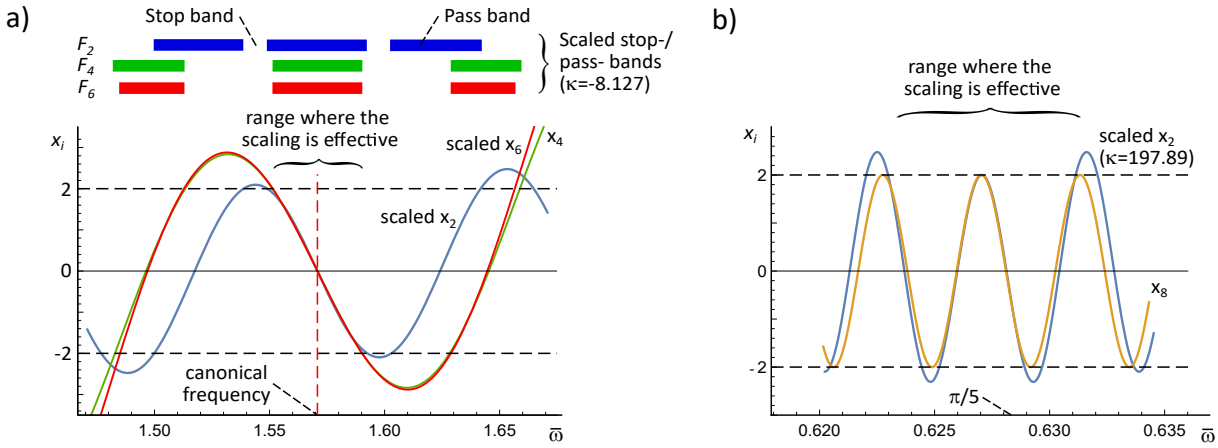

Figure 6: Canonical SM rod with $\mathcal{C}_1 = 5$ (Family no. 1). a) Plot of traces $x_2(\omega/\kappa)$, $x_4(\omega)$, $x_6(\kappa\omega)$ ($\kappa = -8.127$) in the neighbourhood of the canonical frequency ($l_A\sqrt{Q_A}\omega_{\mathcal{C}_1} = \pi/2$); b) plot of traces $x_2(\omega/\kappa)$ and $x_8(\omega)$ ($\kappa = 197.89$) in the neighbourhood of the point $\bar{\omega} = l_A\sqrt{Q_A}\omega = \pi/5$ where a 6-point periodic orbit is detected (see Fig. 3).

the other two eigenvalues and its value will be also indicated from now as κ_p, or simply κ, as there is no risk of confusing it with another quantity.

Imagine now to decompose $\delta\mathbf{r}_i$ with respect to the basis $\{\mathbf{g}^+, \mathbf{g}^-, \mathbf{g}^\star\}$ as $\delta\mathbf{r}_i = \xi^+\mathbf{g}^+ + \xi^-\mathbf{g}^- + \xi^\star\mathbf{g}^\star$. Therefore, by applying eq. (26), it turns out that $\delta\hat{\mathbf{r}}_{i+p} = \bar{\mathbf{A}}_p\delta\mathbf{r}_i = \kappa_p\xi^+\mathbf{g}^+ + \xi^-/\kappa_p\mathbf{g}^- + \xi^\star\mathbf{g}^\star$. Due to the dominance of the highest eigenvalue,

$$\delta\hat{\mathbf{r}}_{i+p} \approx \kappa_p\xi^+\mathbf{g}^+ \approx \kappa_p\delta\mathbf{r}_i. \tag{28}$$

Note that, due to the fact that we are analysing a saddle point, eigenvector $\mathbf{g}^\star$ is orthogonal to the tangent plane at $P_{\bar{j}}$ whereas the other two eigenvectors span the tangent plane. Therefore, vector $\kappa_p\xi^+\mathbf{g}^+$ belongs to the tangent plane itself.

For periodic orbits other than those originating in the neighbourhood of a saddle point, the methodology is similar and based on the linearisation about one of the point of the orbit.

4.2 Scaling of the frequency spectra

Examples of the interpretation of the linearisation of the trace map as a method to explain scaling of the frequency spectra of canonical SM rods are reported in Figs. 6 and 7, which analyse self-similar portions of the stop-/pass-band layouts displayed in Figs. 3 and 4, respectively. In detail, in Fig. 6a) the neighbourhood of the canonical frequency ($l_A\sqrt{Q_A}\omega_{\mathcal{C}_1} = \pi/2$), at which a 2-point periodic orbit occurs, is investigated.

With reference to the linearisation procedure, the involved saddle point is here $P_{\bar{j}} = P_5$, where the two vanishing coordinates correspond to x_2 and x_3. To the first order,

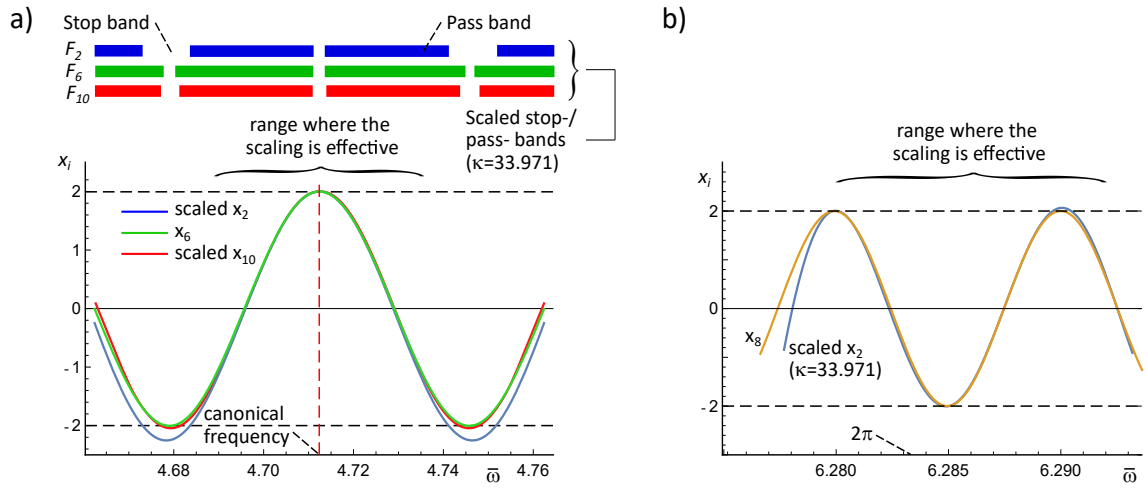

Figure 7: Canonical SM rod with $\mathcal{C}_3 = 2/3$ (Family no. 3). a) Plot of traces $x_2(\omega/\kappa)$, $x_6(\omega)$, $x_{10}(\kappa\omega)$ ($\kappa = 33.971$) in the neighbourhood of the canonical frequency ($l_A\sqrt{Q_A}\omega_{\mathcal{C}_3} = 3\pi/2$); b) plot of traces $x_2(\omega/\kappa)$ and $x_6(\omega)$ ($\kappa = 33.971$) in the neighbourhood of the point $\bar{\omega} = l_A\sqrt{Q_A}\omega = 2\pi$ where a 4-point periodic orbit is detected (see Fig. 3).

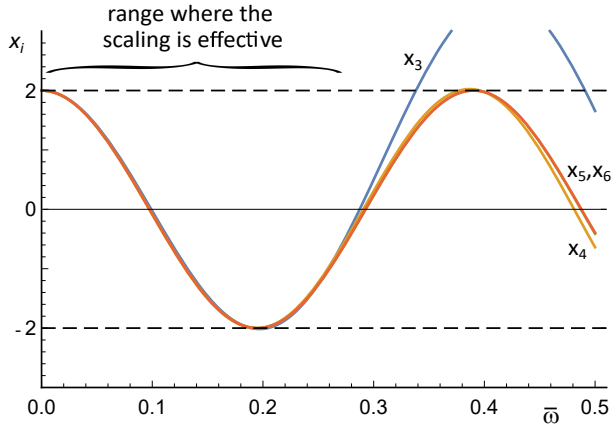

Figure 8: Canonical SM rod with $\mathcal{C}_1 = 5$ (Family no. 1): plot of traces $x_3(\omega)$, $x_4(\kappa\omega)$, $x_5(\kappa^2\omega)$, $x_6(\kappa^3\omega)$ ($\kappa = \sigma_s$) in the neighbourhood of $\omega = 0$ where a fixed-point orbit, $R_0 = (2, 2, 2)$, is present. The plots of x_5 and x_6 are almost indistinguishable.

vector $\delta\mathbf{r}_2(\delta\omega) = \bar{R}_2 - P_5$ can be written as

$$\delta\mathbf{r}_2(\delta\omega) \approx \boldsymbol{\gamma}\delta\omega, \tag{29}$$

where $\boldsymbol{\gamma} = \mathsf{grad}_\omega \delta\mathbf{r}_2$. Approximation (29) lies in the tangent plane spanned by coordinates x_2 and x_3, therefore, we can say that, in the neighbourhood of the canonical frequency, $x_2 \approx \gamma_2\delta\omega$ and $x_3 \approx \gamma_3\delta\omega$, where γ_k ($k = 2, 3$) are the projections of vector $\boldsymbol{\gamma}$ onto axes x_k ($k = 2, 3$). Focusing on x_2, it is clear that after a 2-point cycle, eq. (28) leads to $x_4 \approx \kappa\gamma_2\delta\omega$ and, by repeating the cycle, $x_6 \approx \kappa^2\gamma_2\delta\omega$. This is exactly what is reported

in Fig. 6a) where traces x_2, x_4, x_6 are scaled accordingly by using the factor $\kappa = -8.127$ (cf. eq. $(27)_1$, evaluated for $\beta = 2.5$); the only difference is that the frequency range reported on the horizontal axis pertains strictly to x_4, therefore x_2 is scaled and plotted as $x_2(\omega/\kappa)$ whereas x_6 is plotted as $x_6(\kappa\omega)$. It is evident that within the range comprised within the brace in the figure, the scaling of traces explains quantitatively very well their behaviour about the canonical frequency. As a consequence, the stop-/pass-band layout can be predicted through scaling about the canonical frequency, as shown on top of Fig. 6a). Note that in this case, and for all canonical SM rods belonging to Family no. 1, the scaling factor can be negative. For Fig. 6b), similar comments can be made, here the focus is the neighbourhood of frequency $\bar{\omega} = \pi/5$, where a 6-point periodic orbit is detected. Therefore, the two represented traces are $x_8(\omega)$ and the scaled $x_2(\omega/\kappa)$, where this time the multiplicative factor is $\kappa = \sigma_s^6 = 197.89$.

Fig. 7a) covers the case belonging to Family no. 3 reported in Fig. 4, where the canonical frequency ($l_A\sqrt{Q_A}\omega_{\mathcal{C}_3} = 3\pi/2$) is the locus of a 4-point periodic orbit. Therefore, the represented traces are $x_6(\omega)$, $x_2(\omega/\kappa)$ and $x_{10}(\kappa\omega)$ with $\kappa = \sigma_s^4 = 33.971$ (cf. eq. $(27)_2$). The feature that distinguishes this example from that in Fig. 6a) is that the function x_2 evaluated at $\omega_{\mathcal{C}_3}$ is not null. We will show however that the scaling factor between the chosen three traces is still κ despite the fact that they are not linear functions of circular frequency in the vicinity of $\omega_{\mathcal{C}_3}$.

The involved saddle point is now P_1 that should be better seen as the point of Kohmoto's surface whose coordinates are $(t_4, x_3, x_2)|_{\omega=\omega_{\mathcal{C}_3}} = (0, 0, 2)$. On the one hand, following the argument presented before, about the canonical frequency, t_4 and x_3 are linear in the frequency, then $t_4 \approx \eta_4\delta\omega$ and $x_3 \approx \gamma_3\delta\omega$; on the other hand, at the lowest order, x_2 can be approximated as $x_2 \approx 2 - \zeta_2\delta\omega^2$ and the invariant as $I \approx \delta\omega^2$ as it can be easy inferred with a Taylor expansion of (15). The use of the above approximations still in (15) yields, to the leading (second) order,

$$\delta\omega^2 = (\eta_4\delta\omega)^2 + (\gamma_3\delta\omega)^2 - 4\zeta_2\delta\omega^2 - 2\eta_4\gamma_3\delta\omega^2, \tag{30}$$

and, finally,

$$4\zeta_2 = (\eta_4 - \gamma_3)^2 - 1, \tag{31}$$

which is a consequence of the recursive relationships between adjacent traces.

Let us turn now our attention to the same saddle point, but evaluated after a cycle of four applications of the trace map, i.e. $(t_8, x_7, x_6)|_{\omega=\omega_{\mathcal{C}_3}} = (0, 0, 2)$. By repeating the argument, we can write

$$t_8 \approx \eta_8\overline{\delta\omega}, \quad x_7 \approx \gamma_7\overline{\delta\omega} \ \text{ and } \ x_6 \approx 2 - \zeta_6\overline{\delta\omega}^2, \tag{32}$$

where

$$\eta_8 \approx \kappa\eta_4 \ \text{ and } \ \gamma_7 \approx \kappa\gamma_3, \tag{33}$$

and the overbar has been added to the independent variable because we need to consider a scaled domain. Our goal is to find the connection between ζ_2 and ζ_6 through the factor κ. In particular, note that in analogy to the case illustrated in Fig. 6a), x_7 (resp. t_8) matches x_3 (resp. t_4) if $\overline{\delta\omega} = \delta\omega/\kappa$. Therefore, we can again consider eq. (30) and substitute the terms of the r.h.s. with those expressed as a function of $\overline{\delta\omega}$, i.e.

$$\delta\omega^2 = (\eta_8\overline{\delta\omega})^2 + (\gamma_7\overline{\delta\omega})^2 - 4\zeta_6\overline{\delta\omega}^2 - 2\eta_8\gamma_7\overline{\delta\omega}^2. \tag{34}$$

Updating the l.h.s. of eq. (34) using $\delta\omega = \kappa\overline{\delta\omega}$ and employing (33) yields

$$\kappa^2[(\eta_4 - \gamma_3)^2 - 1]/4 = \zeta_6, \tag{35}$$

which transforms to $\kappa^2\zeta_2 = \zeta_6$ with the help of eq. (31). Therefore, we have proofed our conjecture; κ enters as a square as it is associated with a second-order term in the Taylor expansion. Note that for the parameters selected in Fig. 7a), $\zeta_6 = 8867.11$ and $\zeta_2 = 7.778$ whose ratio has square root equal to 33.76, a value very close to κ.

In Fig. 7b), the neighbourhood of $\bar{\omega} = 2\pi$ is analysed. As at this frequency a 4-point periodic orbit takes place, trace $x_6(\omega)$ and the scaled one $x_2(\omega/\kappa)$ are sketched where $\kappa = 33.971$ is still the scaling factor obtained from the linearisation of the trace map.

Fig. 8 illustrates the effectiveness of the presented method to explain scaling by sketching the plots of the functions of four scaled traces (x_3 to x_6, the represented domain is that of the function $x_3(\omega)$) at the origin ($\omega = 0$) where a fixed-point orbit is present (see case i) in Sect. 3.2). The scaling factor is now $\kappa = \sigma_s$.

5 Conclusions

Periodic quasicrystalline-based phononic waveguides can be studied as a collection of elementary cells whose frequency spectra are connected through a function, the Kohmoto's invariant, that is an invariant of the set and depends only on the wave frequency. A typical expression of this close connection is the self similarity of spectra in the neighbourhood of specific frequencies. It has been shown by the Authors in an earlier paper [24] that for a notable quasicrystalline sequence, i.e. the standard, or *golden-mean* Fibonacci sequence, there exist special configurations of the elementary cells, called *canonical configurations*, that display periodic frequency spectra.

The goal of this paper is to study the existence of similar canonical arrangementd for *silver-mean* Fibonacci phononic waveguides that are based on one of the possible generalisation of the standard Fibonacci chain. We give a positive answer to the initial objective and the outcomes of the present research can be listed as follows:

- the dispersive properties of harmonic axial waves in SM rods are fully determined by studying the variation of the traces of the transmission matrices as a function

of the angular frequency. For any value of the frequency, the traces corresponding to three arbitrary subsequent elementary cells are related through a recursive relationship that is different from that ruling standard, or *golden-mean*, structures [17], but characterised by the same Kohmoto's invariant. This allows us to represent geometrically the traces as coordinates of points which describe orbits on the 3D surface defined by the invariant;

- similarly to the standard Fibonacci sequence, for SM rods three families of *canonical configurations* can be defined, each of them associated with a specific rational value of the quantity $\mathcal{C} = l_B/l_A\sqrt{Q_B/Q_A}$. Canonical SM rods display a periodic frequency spectra, however, as distinct from the case addressed by Gei et al. [24], at the canonical frequency, Family no. 1 displays a two-point periodic orbit on the Kohmoto's surface, whereas for Families no. 2 and 3 periodic orbits involve four saddle points;

- in general, there exist some frequencies at which additional periodic orbits are present. For all these frequencies $\hat{\omega}$, the Kohmoto's invariant vanishes (i.e. $I(\hat{\omega}) = 0$). This could be detected in several cases depending on the value of the ratio $\mathcal{C}$ which determines the modulation of the invariant with respect to ω. The following two universal cases are found: (i) at $\omega = 0, 4\,\omega_{\mathcal{C}_r}$, where $\omega_{\mathcal{C}_r}$ is the canonical frequency, a *fixed-point* exist; (ii) at $\omega = 2\,\omega_{\mathcal{C}_r}$, a two-point periodic orbit occurs;

- a self-similar layout of the stop-/pass-band diagram is observed for canonical SM rods. Analytical scaling factors capturing this pattern are derived through the linearisation of the trace map about the relevant periodic orbits. Depending on the number of points p composing the orbits, portions of the spectra corresponding to elementary cells of the order i and $i + p$ are related by means of these factors. A detailed analysis of the frequency ranges where the scaling is effective is performed;

- we finally propose a different way to represent the sequence of pass bands and stop bands by following the trajectories of points at varying frequency on a 2D projection of the Kohmoto's surface.

The exceptional self-similar properties of the spectrum of two-phase canonical silver-mean rods here illustrated could be applied to realise phononic waveguides possessing stop and pass bands of tunable width centered at a selected frequency. The filtering properties of these devices can be predicted and optimised by means of the novel analytical approach introduced in the paper.

Acknowledgements. AKMF acknowledges support from Embassy of Lybia (ref.

no. 13556). LM acknowledges support from Cardiff University. MG is grateful to the support provided by University of Trieste through grant FRA2021 'NEO-PHONON'.

References

[1] M. Brun, S. Guenneau, A. B. Movchan, and D. Bigoni. Dynamics of structural interfaces: filtering and focussing effects for elastic waves. *J. Mech. Phys. Solids*, 58:1212–1224, 2010.

[2] G. Shmuel and R. Band. Universality of the frequency spectrum of laminates. *J. Mech. Phys. Solids*, 92:127–136, 2016.

[3] G. Trainiti, Y. Xia, J. Marconi, G. Cazzulani, A. Erturk, and M. Ruzzene. Time-periodic stiffness modulation in elastic metamaterials for selective wave filtering: Theory and experiment. *Phys. Rev. Lett.*, 122:124301, 2019.

[4] S. Tol, F. L. Degertekin, and A. Erturk. Structurally embedded reflectors and mirrors for elastic wave focusing and energy harvesting. *J. Appl. Phys.*, 122:164503, 2017.

[5] T. P. Waters. A chirp excitation for focussing flexural waves. *J. Sound Vibr.*, 439:113–128, 2019.

[6] A.N. Norris. Acoustic cloaking theory. *Proc. Roy. Soc. A*, 464(2097):2411–2434, 2008.

[7] M. Brun, S. Guenneau, and A. B. Movchan. Achieving control of in-plane elastic waves. *Appl. Phys. Lett.*, 94:061903, 2009.

[8] A. Srivastava. Metamaterial properties of periodic laminates. *J. Mech. Phys. Solids*, 96:252–263, 2016.

[9] J. R. Willis. Negative refraction in a laminate. *J. Mech. Phys. Solids*, 97:10–18, 2016.

[10] L. Morini, Y. Eyzat, and M. Gei. Negative refraction in quasicrystalline multilayered metamaterials. *J. Mech. Phys. Solids*, 124:282–298, 2019.

[11] E. Riva, M. Di Ronco, A. Elabd, G. Cazzulani, and F. Braghin. Non-reciprocal wave propagation in discretely modulated spatiotemporal plates. *J. Sound Vibr.*, 471:115186, 2020.

[12] Z.-N. Li, Y.-Z. Wang, and Y.-S. Wang. Tunable mechanical diode of nonlinear elastic metamaterials induced by imperfect interface. *Proc. R. Soc. A*, 477:20200357, 2020.

[13] M. Gei. Wave propagation in quasiperiodic structures, stop/pass band distribution and prestress effects. *Int. J. Solids Struct.*, 47:3067–3075, 2010.

[14] V. S. Sorokin. Longitudinal wave propagation in a one-dimensional quasi-periodic waveguide. *Proc. R. Soc. A*, 475:20190392, 2019.

[15] R. K. Pal, M. I. N. Rosa, and M. Ruzzene. Topological bands and localized vibration modes in quasiperiodic beams. *New J. Phys.*, 21:093017, 2019.

[16] Y. Xia, A. Erturk, and M. Ruzzene. Topological edge states in quasiperiodic locally resonant metastructures. *Phys. Rev. Appl.*, 13:014023, 2020.

[17] L. Morini and M. Gei. Waves in one-dimensional quasicrystalline structures: dynamical trace mapping, scaling and self-similarity of the spectrum. *J. Mech. Phys. Solids*, 119:83–103, 2018.

[18] L. Morini, Z. G. Tetik, G. Shmuel, and M. Gei. On the universality of the frequency spectrum and band-gap optimization of quasicrystalline-generated structured rods. *Phil. Trans. R. Soc. A*, 378:20190240, 2019.

[19] A.N. Poddubny and E.L. Ivchenko. Photonic quasicrystalline and aperiodic structures. *Physica E*, 43:1871–1895, 2010.

[20] H.-F. Zhang. Investigations on the two-dimensional aperiodic plasma photonic crystals with fractal Fibonacci sequence. *AIP Advances*, 7:075102, 2017.

[21] M. Kohmoto and Y. Oono. Cantor spectrum for an almost periodic Schroedinger equation and a dynamical map. *Phys. Lett.*, 102A:145–148, 1984.

[22] M. Holzer. Nonlinear dynamics and localization in a class of one-dimensional quasicrystals. *Phys. Rev. B*, 38:5756–5760, 1988.

[23] M. Kolar and M.K. Ali. Generalized Fibonacci superlattices, dynamical trace maps, and magnetic excitations. *Phys. Rev. B*, 39:426–432, 1989.

[24] M. Gei, Z. Chen, F. Bosi, and L. Morini. Phononic canonical quasicrystalline waveguides. *Appl. Phys. Lett.*, 116:241903, 2020.

[25] M. Kolar. New class of one dimensional quasicrystals. *Phys. Rev. B*, 47:5498–5492, 1993.

[26] W. Steurer. Twenty years of structure research on quasicrystals. Part I. Pentagonal, octagonal, decagonal and dodecagonal quasicrystals. *Acta Crystals*, 219:391–446, 2004.

[27] W. Steurer and S. Deloudi. Fascinating quasicrystals. *Acta Crystals*, A64:1–11, 2008.

[28] J. Lekner. Light in periodically stratified media. *J. Opt. Soc. Am. A*, 11:2892–2899, 1994.

[29] F. Romeo and A. Luongo. Invariant representation of propagation properties for bi-coupled periodic structures. *Journal of Sound and Vibration*, 257:869–886, 2002.

[30] G. Carta and M. Brun. Bloch–Floquet waves in flexural systems with continuous and discrete elements. *Mechanics of Materials*, 87:11–26, 2015.